Microscopic description of hexadecapole collectivity in even-even rare-earth nuclei near $N = 90$

L. Lotina [1,*] and K. Nomura [2,3,†]

[1]*Department of Physics, Faculty of Science, University of Zagreb, HR-10000 Zagreb, Croatia*
[2]*Department of Physics, Hokkaido University, Sapporo 060-0810, Japan*
[3]*Nuclear Reaction Data Center, Hokkaido University, Sapporo 060-0810, Japan*

We present an extensive study of hexadecapole correlations in the rare-earth region near $N = 90$ and the effects these correlations have on various nuclear properties, such as the low-energy spectra, as well as quadrupole, hexadecapole, and monopole transition strengths. In order to examine hexadecapole correlations, we employ a mapped sdg interacting boson model, with parameters derived from a self-consistent mean-field calculations with a relativistic energy density functional. We apply this model to even-even isotopes of Nd, Sm, Gd, Dy, and Er ($Z = 60$–68) with neutron numbers $N = 84$–96. The obtained results show a good agreement with the experiment. By comparing the results with the ones obtained from a simpler mapped sd interacting boson model, we show that the inclusion of the hexadecapole degree of freedom via the g boson is necessary to improve the results of the $J^\pi \geqslant 6^+$ yrast energies in the nuclei with $N = 84$ and 86, being near the neutron shell closure. The sdg interacting boson model increases the quadrupole transition strengths between yrast states in the $N = 90$ and 92 well deformed nuclei, which is in good agreement with the experiment for most of those isotopes. The presence of g bosons does have an important effect on hexadecapole transition strengths, although experimental data for such transitions are limited. The obtained monopole transition strengths do not differ significantly from the ones obtained from the simpler sd model.

I. INTRODUCTION

Nuclear deformations play an important role in describing various nuclear properties [1,2], e.g., excitation energies and decays. The dominant deformations in nuclei, the quadrupole ones, have been extensively studied. More and more attention is recently being paid to higher-order deformations, such as the octupole and hexadecapole ones. The effects of hexadecapole correlations are often overshadowed by large quadrupole effects. Nevertheless, they have been found to exist in a wide spectrum of nuclei, ranging from light nuclei [3] to heavy nuclei [4]. The main effect of hexadecapole correlations on the low-lying energy spectrum of the nucleus is the appearance of the low-lying $K = 4^+$ band with an enhanced $B(E4; 4^+ \to 0^+)$ transition strength. Another effect can be observed in even-even rare-earth nuclei near the $N = 82$ shell closure, where the ratio of the ground-state band energies $R_{4/2} = E_x(4^+)/E_x(2^+)$ becomes less than 2. Besides that, hexadecapole deformations were shown to play a significant role in heavy ion collisions [4] and fission [5], and are predicted to have an influence on the neutrinoless double beta decay matrix elements in open shell nuclei [6]. All of this provides us with a good reason to study hexadecapole correlations in nuclei and their effects on the low-lying excitation spectra and transitions.

A useful framework for studying the effects of nuclear deformations is the interacting boson model (IBM) [7]. In the simplest version of the IBM, the nucleus can be viewed as a system composed of a doubly magic core nucleus, and valence nucleons grouped into s ($L^\pi = 0^+$) and d ($L^\pi = 2^+$) bosons. The main assumption of the model is that the main contribution to the low-lying excitation energy spectra comes from the pairing correlations between aforementioned bosons. In the version of the model called IBM-1, it is assumed that the neutron and proton bosons are identical [7]. This model has been successfully used to study the effects of deformations in nuclei [8]. Since the IBM is a phenomenological model, in recent times, a method was developed that derives the parameters of the IBM Hamiltonian from a self-consistent mean-field (SCMF) model with energy density functionals (EDFs) [9]. This method has been successfully applied in studying quadrupole [9–12] and octupole correlations [13,14] in nuclei. The inclusion of the hexadecapole degree of freedom in the IBM is done by the inclusion of the g boson with $L^\pi = 4^+$, whose importance in the IBM has been extensively studied [8,15–21]. While the sdg-IBM has been extensively studied as a phenomenological model, it is useful to study the model through a more microscopic picture, e.g., the aforementioned mapping method, since that could lead us to a better understanding of the microscopic origin of the hexadecapole collectivity in nuclei.

In the preceding article [22], we explored the hexadecapole collectivity in $^{148-160}$Gd isotopes by using the sdg-IBM-1 with the Hamiltonian parameters being derived by the mapping

―――――――
*llotina.phy@pmf.hr
†nomura@sci.hokudai.ac.jp

method of Ref. [9], and showed the validity and usefulness of such approach. The aim of the present article is to extend the study to a wider range of even-even rare-earth isotopes, $^{144-156}$Nd, $^{146-158}$Sm, $^{148-160}$Gd, $^{150-162}$Dy, and $^{152-164}$Er. We choose the rare-earth isotopes for our study due to the fact that hexadecapole correlations were observed in that region [1,23–27], as well as due to the fact that triaxiality does not play a significant role in these isotopes, as is evident from SCMF calculations with the Skyrme force [10] and Gogny force [28]. By comparing our model with a simpler mapped sd-IBM-1, we explore the effects of hexadecapole correlations on the low-lying excitation energy spectra of these isotopes, and also on the monopole, quadrupole, and hexadecapole transition strengths.

The paper is organized as follows. In Sec. II we describe our model. Section III gives the quadrupole-hexadecapole potential energy surfaces for the studied nuclei. Results of the spectroscopic properties, including the excitation spectra of low-lying states and the electric quadrupole, hexadecapole, and monopole transition properties, are discussed in Sec. IV. A summary of the main results and some perspectives for future work are given in Sec. V.

II. MODEL DESCRIPTION

We begin our analysis with the SCMF calculations. The model employed for SCMF calculations is the multidimensionally constrained relativistic mean-field (MDC-RMF) model [29–31], which allows one to set constraints on various deformation parameters. For our analysis, we carried out the SCMF calculations for axially symmetric shapes in the (β_2, β_4) plane, by setting the constraints on the mass quadrupole Q_{20} and hexadecapole Q_{40} moments. The dimensionless quadrupole β_2 and hexadecapole β_4 deformation parameters are related to the mass moments through the relation

$$\beta_\lambda = \frac{4\pi}{3AR^\lambda}\langle \hat{Q}_{\lambda 0}\rangle \qquad (1)$$

with $R = 1.2A^{1/3}$ fm. The quadrupole-hexadecapole constrained potential energy surfaces (PESs) are calculated within the relativistic Hartree-Bogoliubov (RHB) framework [32,33], with the chosen energy density functional being the density-dependent point-coupling (DD-PC1) interaction [33,34], combined with the separable pairing interaction of finite range developed in Ref. [35]. A detailed description of the MDC-RMF model can be found in Refs. [30,31].

Due to the fact that SCMF calculations necessarily break several symmetries, these calculations alone cannot be used to study excited states and transitions in the nucleus. To study those properties of the nucleus, we use the sdg-IBM-1 model. A simple version of the sdg-IBM-1 Hamiltonian is given by the following relation, similar to the one from [20]:

$$\hat{H}_{sdg} = \epsilon_d \hat{n}_d + \epsilon_g \hat{n}_g + \kappa_2 \hat{Q}^{(2)} \cdot \hat{Q}^{(2)} + \kappa_4 \hat{Q}^{(4)} \cdot \hat{Q}^{(4)}. \qquad (2)$$

The first two terms represent the d and g boson number operators, $\hat{n}_d = d^\dagger \cdot \tilde{d}$ and $\hat{n}_g = g^\dagger \cdot \tilde{g}$. The second term represents the quadrupole-quadrupole interaction with the quadrupole

operator, defined as

$$\hat{Q}^{(2)} = (s^\dagger \tilde{d} + d^\dagger s) + \chi_{dd}^{(2)}(d^\dagger \times \tilde{d})^{(2)}$$
$$+ \chi_{dg}^{(2)}(d^\dagger \times \tilde{g} + g^\dagger \times \tilde{d})^{(2)} + \chi_{gg}^{(2)}(g^\dagger \times \tilde{g})^{(2)}, \quad (3)$$

while the last term represents the hexadecapole-hexadecapole interaction, with the hexadecapole operator defined as

$$\hat{Q}^{(4)} = (s^\dagger \tilde{g} + g^\dagger s) + \chi_{dd}^{(4)}(d^\dagger \times \tilde{d})^{(4)}$$
$$+ \chi_{dg}^{(4)}(d^\dagger \times \tilde{g} + g^\dagger \times \tilde{d})^{(4)} + \chi_{gg}^{(4)}(g^\dagger \times \tilde{g})^{(4)}. \quad (4)$$

Since this Hamiltonian is too complex, due to the number of parameters it contains, a simplification can be made by assuming three symmetry limits, U(5) ⊗ U(9), SU(3), and SO(15), which leads to a Hamiltonian [21]

$$\hat{H}_{sdg} = \epsilon_d \hat{n}_d + \epsilon_g \hat{n}_g + \kappa \hat{Q}^{(2)} \cdot \hat{Q}^{(2)} + \kappa(1-\chi^2)\hat{Q}^{(4)} \cdot \hat{Q}^{(4)}$$
$$(5)$$

with

$$\hat{Q}^{(2)} = (s^\dagger \tilde{d} + d^\dagger s) + \chi\left[\frac{11\sqrt{10}}{28}(d^\dagger \times \tilde{d})^{(2)}\right.$$
$$\left. - \frac{9}{7}(d^\dagger \times \tilde{g} + g^\dagger \times \tilde{g})^{(2)} + \frac{3\sqrt{55}}{14}(g^\dagger \times \tilde{g})^{(2)}\right] \quad (6)$$

and

$$\hat{Q}^{(4)} = s^\dagger \tilde{g} + g^\dagger s \qquad (7)$$

being the quadrupole and hexadecapole operators, respectively.

The parameters ϵ_d, ϵ_g, κ, and χ are determined by the mapping procedure [9]. The first step is connecting the IBM to the geometric model by calculating the expectation value of the Hamiltonian in a coherent state $|\phi\rangle \propto (1 + \tilde{\beta}_2 d_0^\dagger + \tilde{\beta}_4 g_0^\dagger)^{N_B}|0\rangle$, with N_B representing the number of bosons, i.e., the number of pairs of valence nucleons, and $|0\rangle$ representing the boson vacuum [21]. For Nd, Sm, Gd, and Dy isotopes, the boson vacuum corresponds to the double shell closures $(N, Z) = (82, 50)$, i.e., the doubly magic nucleus ^{132}Sn, while for the Er isotopes, since the valence neutrons are considered hole-like, the corresponding boson vacuum is taken to be $(N, Z) = (82, 82)$. The expectation value, $\langle\phi|\hat{H}|\phi\rangle/\langle\phi|\phi\rangle$, gives us the PES of the IBM, and is denoted $E_{IBM}(\tilde{\beta}_2, \tilde{\beta}_4)$, with $\tilde{\beta}_2$ and $\tilde{\beta}_4$ being boson analogs of the quadrupole β_2 and β_4 deformations, respectively. The parameters of the Hamiltonian are fitted so that the energy surface of the IBM approximates the PES obtained from the SCMF calculations, $E_{SCMF}(\beta_2, \beta_4)$, in the vicinity of the minimum:

$$E_{SCMF}(\beta_2, \beta_4) \approx E_{IBM}(\tilde{\beta}_2, \tilde{\beta}_4). \qquad (8)$$

Following the method of Refs. [9,14], the relation between bosonic and fermionic deformation parameters is assumed to be linear, $\tilde{\beta}_2 = C_2\beta_2$, $\tilde{\beta}_4 = C_4\beta_4$. This leaves us with six parameters in total to be determined. In the case of lighter rare-earth isotopes, Nd and Sm, the Hamiltonian from Eq. (6) is shown to be inadequate to reproduce the SCMF PES, due to the obtained ratios $\beta_4^{min}/\beta_2^{min}$ being larger than in heavier rare-earth isotopes. To solve this problem, an independent

parameter σ was introduced in the quadrupole operator of Eq. (6) as

$$\hat{Q}^{(2)} = (s^\dagger \tilde{d} + d^\dagger s) + \chi \left[\frac{11\sqrt{10}}{28} (d^\dagger \times \tilde{d})^{(2)} \right.$$
$$\left. - \frac{9}{7}\sigma (d^\dagger \times \tilde{g} + g^\dagger \times \tilde{g})^{(2)} + \frac{3\sqrt{55}}{14} (g^\dagger \times \tilde{g})^{(2)} \right],$$
(9)

with constraint $-1 \leqslant \chi\sigma \leqslant +1$. If $\chi = \sigma = +1$, the quadrupole operator corresponds to the generator of the SU(3) algebra [36]. It should be noted that, while the hexadecapole terms and the $(g^\dagger \times \tilde{g})^{(2)}$ are included in the Hamiltonian, their contribution to the IBM PES, as well as to the excitation energies, is minimal, and they could, in principle, be omitted from the Hamiltonian.

In order to study the effects of hexadecapole correlations in nuclei, the sdg IBM has to be compared with a simpler sd IBM, with a Hamiltonian given by the relation [7]

$$\hat{H}_{sd} = \epsilon_d \hat{n}_d + \kappa \hat{Q}^{(2)} \cdot \hat{Q}^{(2)},$$
(10)

with

$$\hat{Q}^{(2)} = s^\dagger \tilde{d} + d^\dagger s + \chi (d^\dagger \times \tilde{d})^{(2)}$$
(11)

being the quadrupole operator. The mapping is performed so that the energy of the sd-IBM approximates the SCMF PES along the $\beta_4 = 0$ line in the vicinity of the minimum [22]:

$$E_{\text{SCMF}}(\beta_2, \beta_4 = 0) \approx E_{\text{IBM}}(\tilde{\beta}_2),$$
(12)

while the relation between the bosonic and fermionic quadrupole deformation parameters is again assumed to be linear, $\tilde{\beta}_2 = C_2^{sd} \beta_2$.

The transition strengths are defined as

$$B(E\lambda; J \to J') = \frac{1}{2J+1} |\langle J' || \hat{T}^{(E\lambda)} || J \rangle|^2,$$
(13)

with $|J\rangle$ and $\langle J'|$ being the wave functions of the initial and final states, respectively. The operators considered are the quadrupole operator

$$\hat{T}^{(E2)} = e_2^{sdg,sd} \hat{Q}^{(2)},$$
(14)

with $\hat{Q}^{(2)}$ corresponding to the quadrupole operator of the sdg- or sd-IBM [Eqs. (2), (6), and (10)]; the hexadecapole operator, defined as

$$\hat{T}^{(E4)} = e_4^{sdg} [s^\dagger \tilde{g} + g^\dagger s + (d^\dagger \times \tilde{d})^{(4)}]$$
(15)

for the sdg-IBM and

$$\hat{T}^{(E4)} = e_4^{sd} (d^\dagger \times \tilde{d})^{(4)}$$
(16)

for the sd-IBM; and the monopole operator, defined as [37]

$$\hat{T}^{(E0)} = (e_n N + e_p Z) \left(\eta \frac{\hat{n}_d}{N_B} + \gamma \frac{\hat{n}_g}{N_B} \right)$$
(17)

for the sdg-IBM and

$$\hat{T}^{(E0)} = (e_n N + e_p Z) \eta \frac{\hat{n}_d}{N_B}$$
(18)

for the sd-IBM. The $e_2^{sdg,sd}$ coefficients are fitted for each isotope so that the experimentally measured transition strength $B(E2; 2_1^+ \to 0_1^+)$ from the first 2^+ state to the ground state should be reproduced. Similarly, the $e_4^{sdg,sd}$ coefficients are fitted to the $B(E4; 4_1^+ \to 0_1^+)$ transition strength. In the case of monopole transitions, following Ref. [37], monopole strengths are defined as

$$\rho(E0) = \frac{\langle J' | \hat{T}^{(E0)} | J \rangle}{eR^2},$$
(19)

with $R = 1.2 A^{1/3}$ fm being the nuclear radius. The parameters $e_{p,n}$ are chosen to be $e_n = 0.50e$, $e_p = e$, following Ref. [37]. However, a different choice from the one in Ref. [37] is made for these parameters, $\eta = \gamma = 0.75$ fm^2. This is due to the fact that the Hamiltonians used in this paper are different from ones used in the aforementioned paper. Most of the experimental data are taken from the National Nuclear Data Center (NNDC) database [38].

III. MAPPING THE SCMF RESULTS ONTO THE IBM SPACE

Figures 1–5 show the PESs of the even-even Nd, Sm, Gd, Dy, and Er isotopes with the neutron number within the range $N = 84$–94, up to 2.7 MeV in energy. The PESs for the $N = 96$ nuclei are not shown due to their similarity to those of the $N = 94$ ones. In addition, the PESs for the Gd isotopes, have already been presented in Ref. [22], but are depicted in Fig. 3 for completeness. From the figures, one can notice that both the quadrupole and hexadecapole deformation parameters increase with the neutron number. The saddle point in the oblate ($\beta_2 < 0$) area is lower in energy for the $N \leqslant 90$ nuclei and can be seen in the PES. For heavier isotopes, the saddle point becomes higher in energy and cannot be seen in the figures. Quadrupole deformations have a similar structural evolution in all isotopes, starting from $\beta_2^{\text{min}} = 0.1$ at $N = 84$, except for the oblate deformed ^{148}Gd ($\beta_2^{\text{min}} = -0.05$), with the maximum $\beta_2^{\text{min}} = 0.35$ calculated for those nuclei with $N = 94$ and 96. It should be noted that, while ^{148}Gd is predicted to be oblate deformed in the ground state, the PES of this nucleus shows a significant softness with respect to both quadrupole and hexadecapole deformation. The structural evolution of hexadecapole deformations is also similar in all isotopes. Larger hexadecapole deformations in the minimum are obtained for lighter nuclei, Nd and Sm, the largest being $\beta_4^{\text{min}} = 0.25$ (^{142,154}Nd, ^{154}Sm). In Gd, Dy, and Er isotopes, the largest hexadecapole deformation in the minimum is $\beta_4^{\text{min}} = 0.15$, present in the $N \geqslant 90$ region. In Dy and Er isotopes, it can be seen that the energy minima for the nuclei in the deformed region (with $N \geqslant 90$) become softer in the β_4 direction compared to those for the $N = 86$ and 88 nuclei. Earlier mean-field-type studies—e.g., those based on the axially deformed Woods-Saxon potential with the hexadecapole degree of freedom [39], the total Routhian surface calculation [40], and a more recent generator coordinate method employing the Gogny EDF to deal with the axial quadrupole-hexadecapole coupling [41]—have also
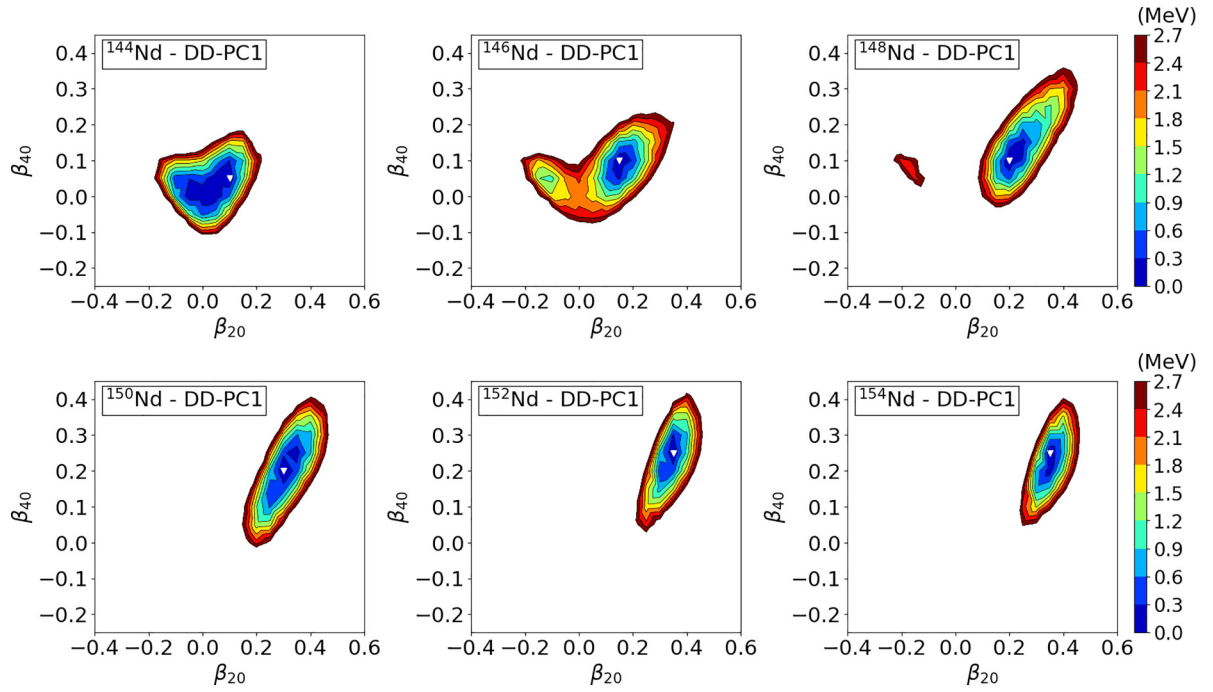
FIG. 1. Axially symmetric quadrupole (β_{20}) and hexadecapole (β_{40}) constrained energy surfaces for the $^{144-154}$Nd isotopes calculated within the relativistic Hartree-Bogoliubov method using the DD-PC1 energy density functional and the pairing force of finite range. Energy difference between neighboring contours is 0.3 MeV, and the absolute minimum is indicated by an open triangle.

found nonzero β_{40} deformations in some rare-earth nuclei near $N = 90$.

The corresponding sdg-IBM PESs are shown in Figs. 6–10. One can see that the mapping procedure reproduces some of the basic properties of the SCMF PES, such as the position of the absolute minimum and the saddle point in the

$N = 84$–90 nuclei. The IBM surface is significantly larger than the SCMF surface, which is a general feature of the IBM due to the restricted boson space of the model. This was already discussed in the case of quadrupole-octupole mapping [14]. The "tail-like" structure that can be seen in the SCMF PES at $N = 88$ in each isotopic chain is also not
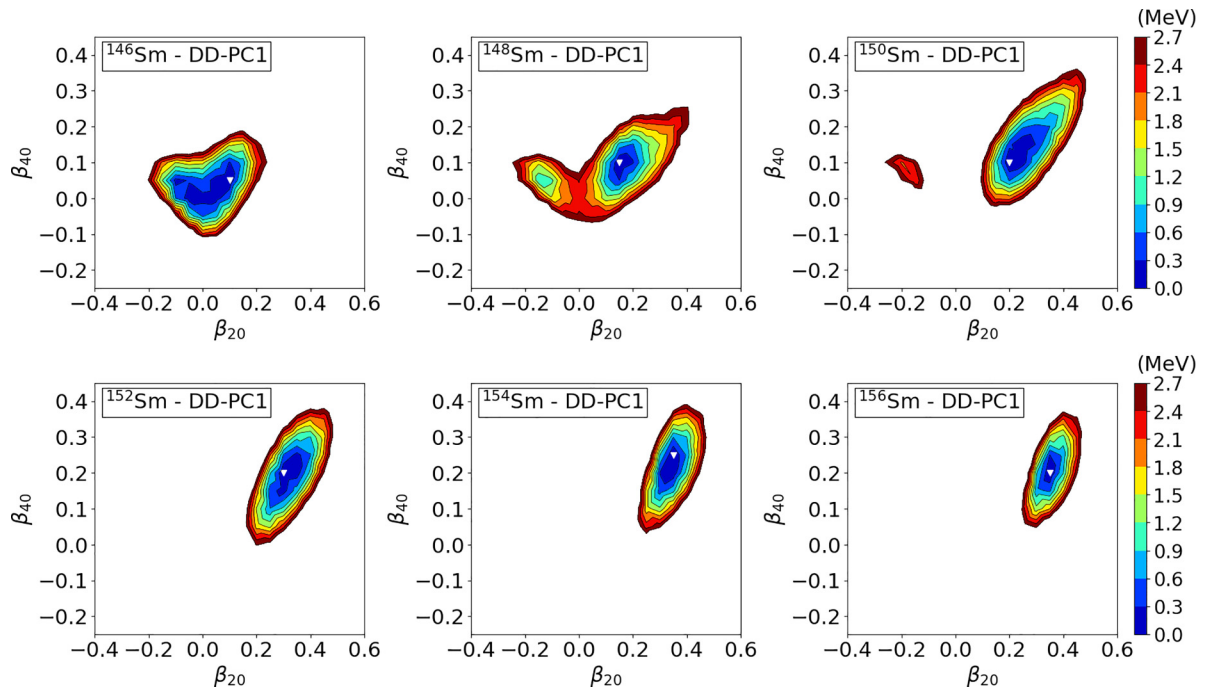
FIG. 2. Same as the caption for Fig. 1, but for $^{146-156}$Sm.
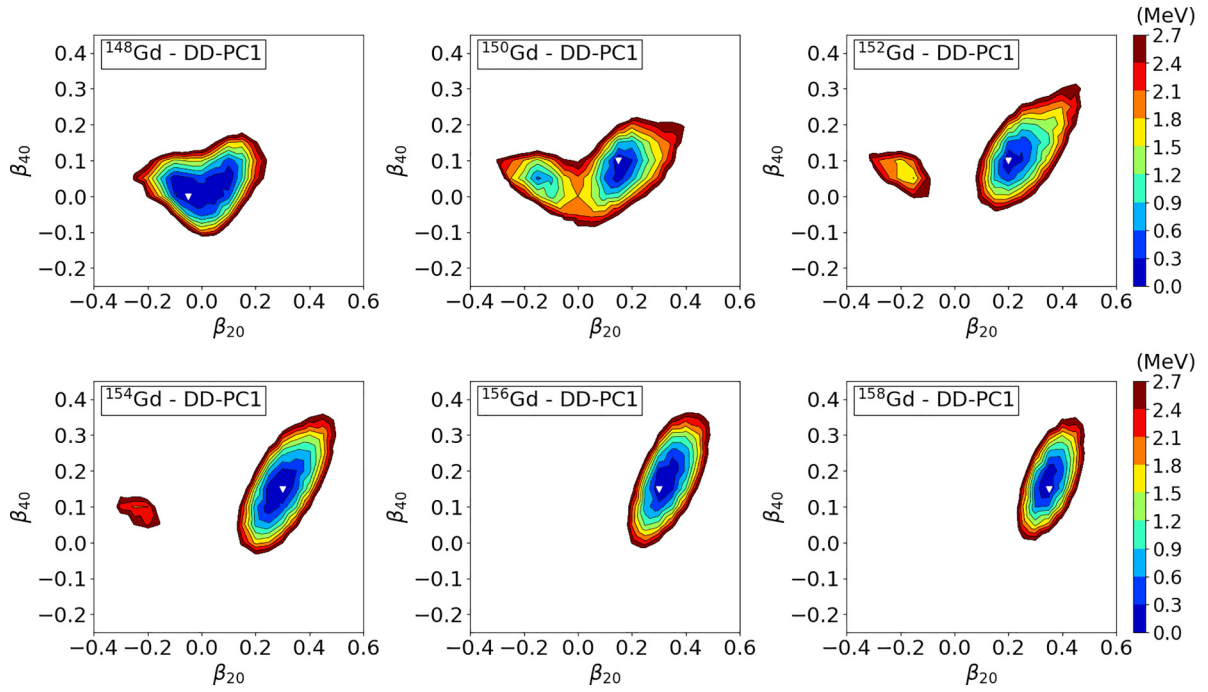
FIG. 3. Same as the caption for Fig. 1, but for $^{148-158}$Gd.

reproduced by the IBM due to the complexities of the SCMF model, which cannot be reproduced by a simple Hamiltonian. While three-body terms would provide an improvement to the IBM PES, such terms are rarely included in the Hamiltonian and are beyond the scope of this study. In the case of the sd-IBM mapping, the goal was to approximately reproduce the energy as a function of the β_2 parameter, with the focus on reproducing the position of the energy minimum, the energy

at $\beta_2 = 0$, and the saddle point in the oblate region. The parameters of the sdg- and sd-IBM are shown in Figs. 11 and 12. The value of parameter σ from Eq. (9), not shown in Fig. 11, is set to $\sigma = 3.5$ for ^{144,146}Nd and ^{146,148}Sm, and $\sigma = 2.8$ for other Nd and Sm isotopes, while for Gd, Dy, and Er isotopes it is set to $\sigma = 1.0$ [see the quadrupole operator in Eq. (6)]. In both the sdg- and sd-IBM, the parameter ϵ_d has a maximum value in the near shell-closure region, and
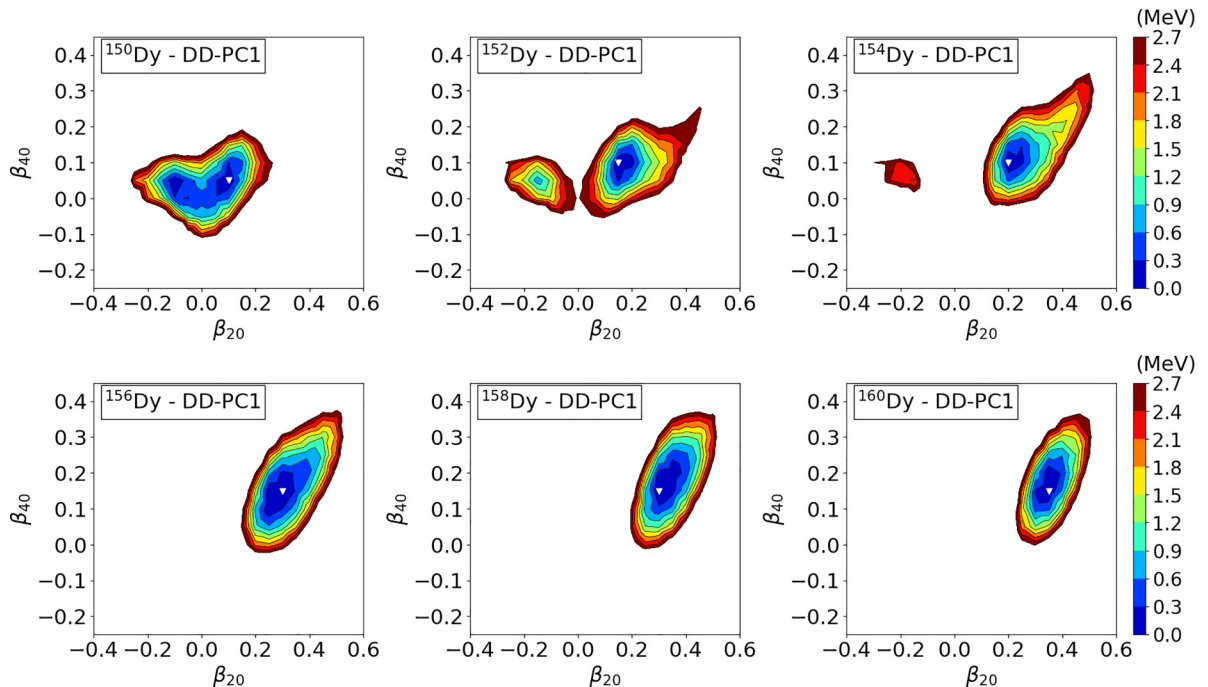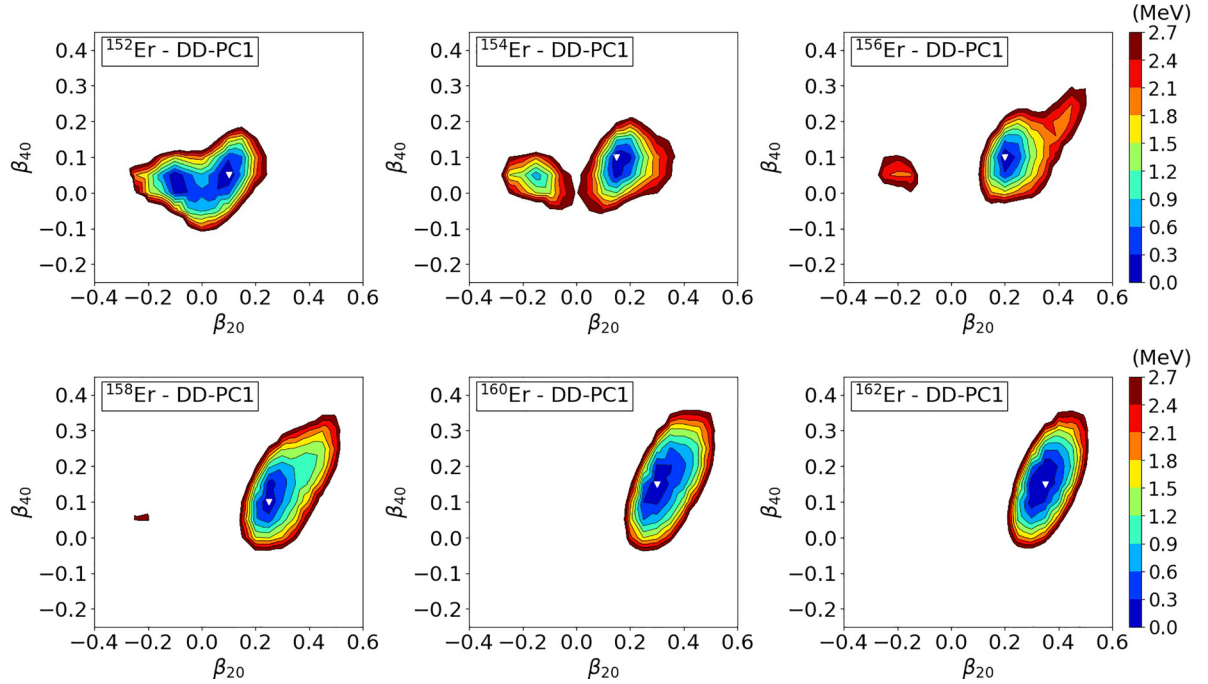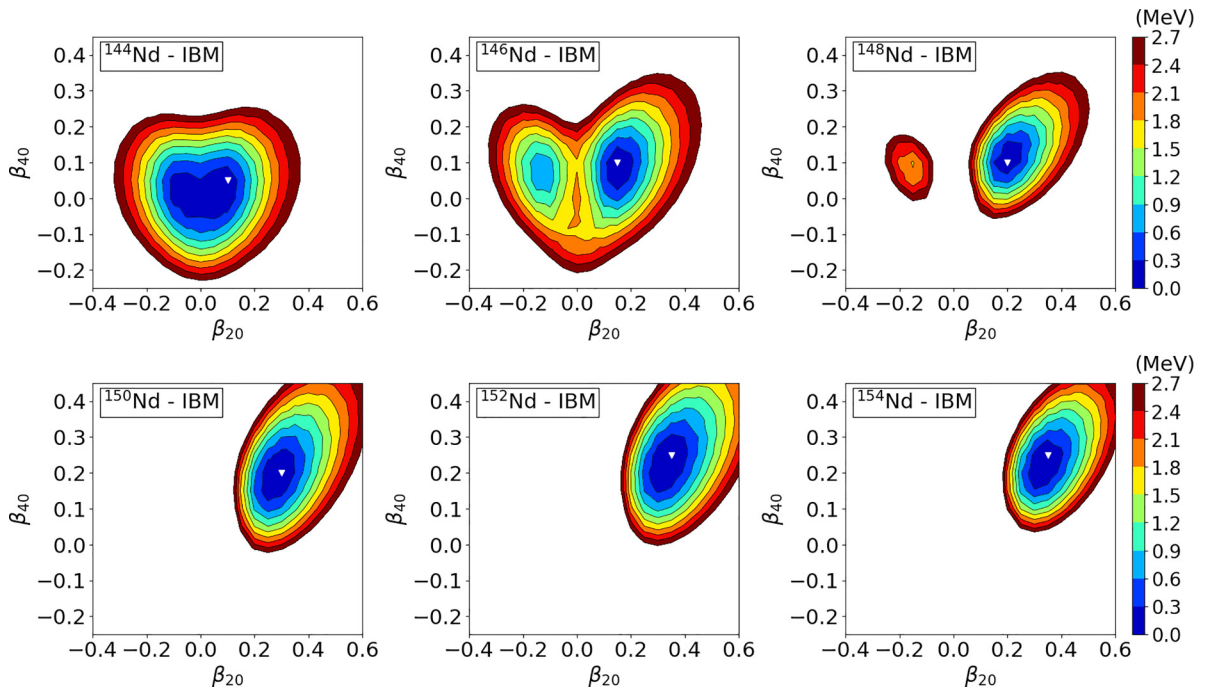

FIG. 4. Same as the caption for Fig. 1, but for $^{150-160}$Dy.

FIG. 5. Same as the caption for Fig. 1, but for $^{152-162}$Er.

its value decreases as we move towards the deformed region. The same happens with the parameter χ. In the sd-IBM, on the other hand, the parameter starts from a positive value in the near shell-closure region and decreases more sharply as we move into the deformed region, achieving significantly lower values from the χ parameter in the sdg-IBM. The C_2 parameter also shows similar evolution in both models. The κ parameter in the sdg-IBM tends to decrease when moving to

the deformed region and increase at the end of the deformed region. This is also the case in the sd-IBM, except in the case of Gd and Dy isotopes, for which κ increases when moving into the deformed region. As for the parameters only present in the sdg-IBM, g boson energy ϵ_g values fluctuate between $\epsilon_g = 1.0$ and $\epsilon_g = 1.3$ MeV, while the C_4 parameter behaves similarly to the C_2 parameter, the difference being that the C_4 parameter values tend to be smaller than the C_2 values for the

FIG. 6. Same as the caption for Fig. 1, but for the mapped sdg-IBM energy surfaces of $^{144-154}$Nd.
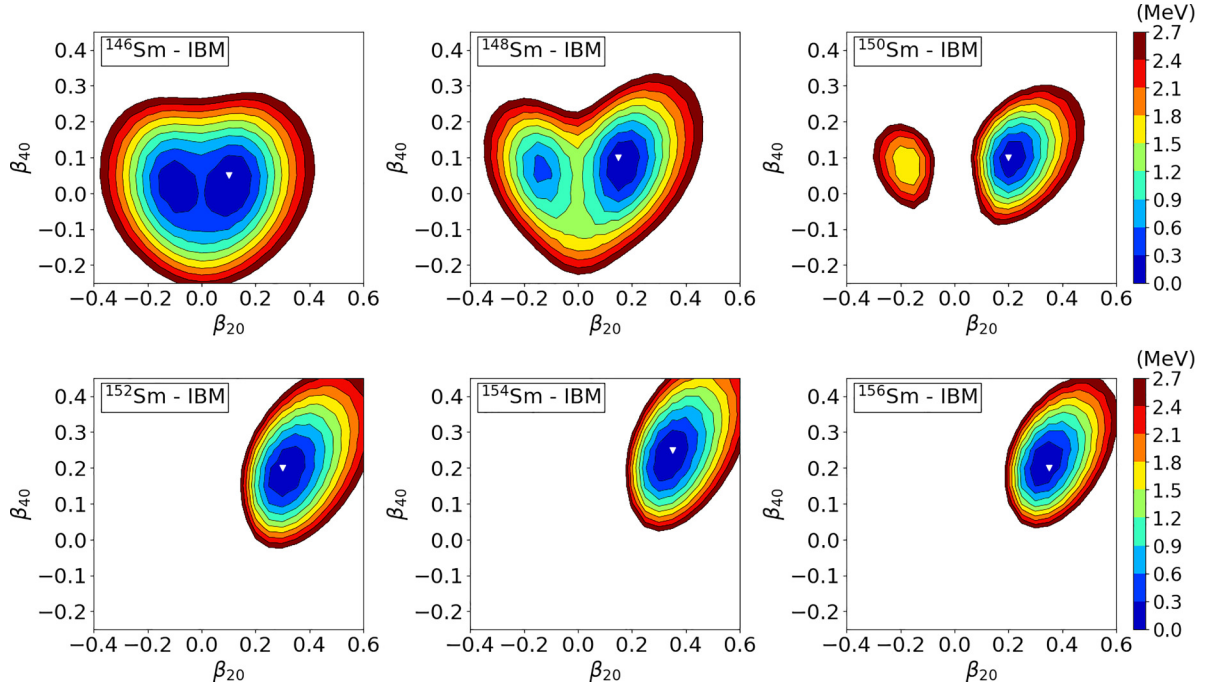
FIG. 7. Same as the caption for Fig. 1, but for the mapped sdg-IBM energy surfaces of $^{146-156}$Sm.

same boson number N_B. Previous phenomenological sdg-IBM calculations on ^{152,154}Sm have set the g boson energy to be $\epsilon_g = 1.4$ and 1.5 MeV, respectively [42], We note, however, that with those values we are not able to reproduce the desired $\beta_4^{\min}$ obtained through the SCMF calculations.

IV. RESULTS OF THE SPECTROSCOPIC CALCULATIONS

In this section, we show the excitation energies and transition strengths. The computer program ARBMODEL [43] is employed to obtain these quantities. The results of the sdg-IBM are compared with the results of the sd-IBM to show the effects of g bosons. The results obtained from both models
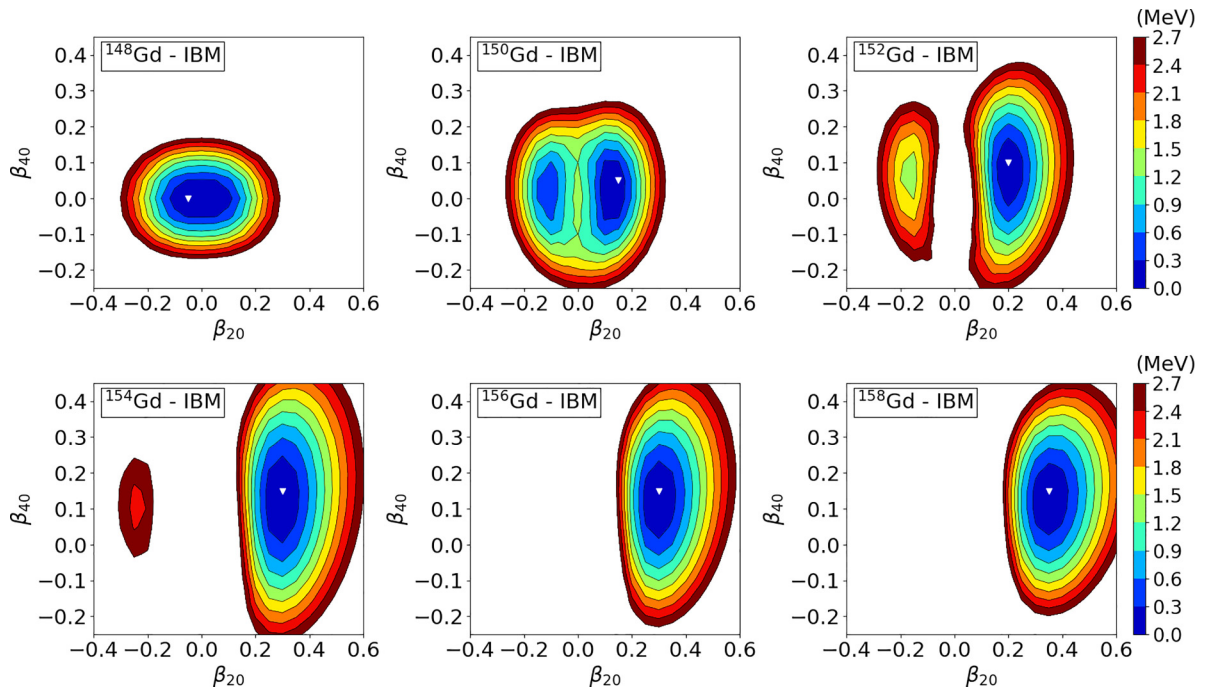

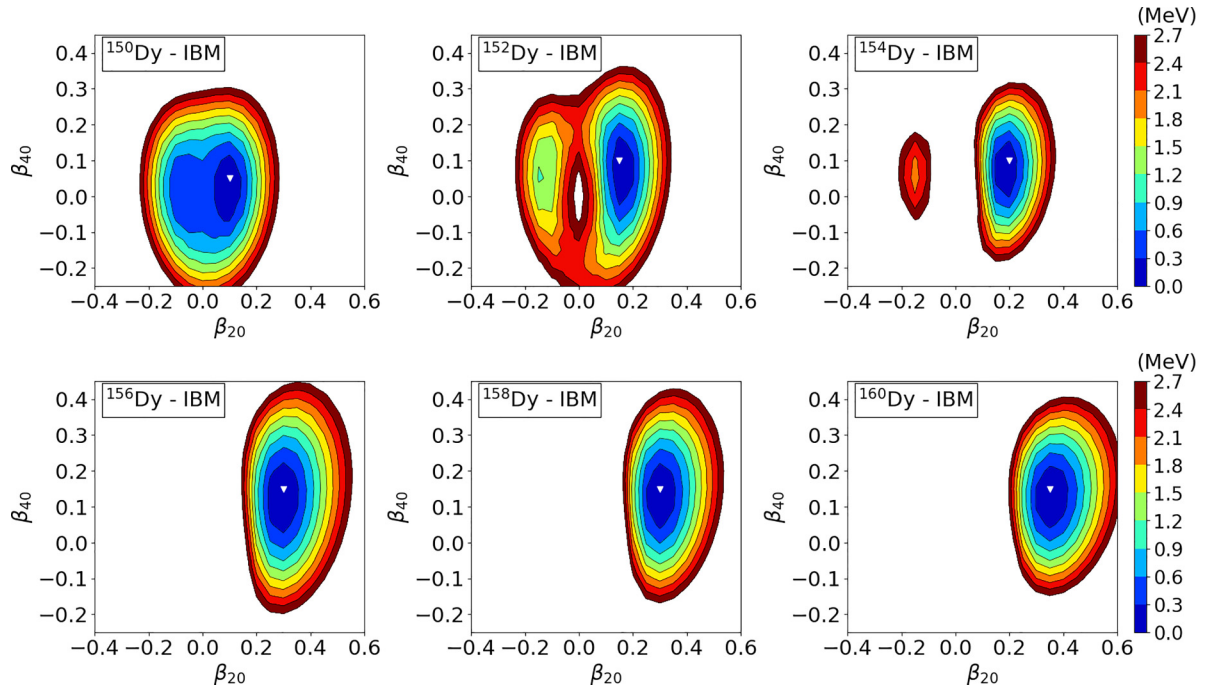FIG. 8. Same as the caption for Fig. 1, but for the mapped sdg-IBM energy surfaces of $^{148-158}$Gd.

FIG. 9. Same as the caption for Fig. 1, but for the mapped sdg-IBM energy surfaces of $^{150-160}$Dy.

are also compared with the experimental data available in the NNDC database [38].

A. Excitation energies

Figure 13 shows the calculated excitation energies of the yrast band states with spin $J^{\pi} = 2^+-14^+$. As can be seen from the figure, the sdg-IBM significantly improves the de-

scription of the $J^{\pi} \geqslant 6^+$ states in the $N \leqslant 88$ nuclei. This can be explained by looking at the expectation value of the g boson number operator, which is for those states calculated to be $\langle \hat{n}_g \rangle \geqslant 1$. The energies of the yrast band states in the near shell-closure region are lowered due to the presence of g bosons.

We also summarize the energy ratios $R_{4/2}$ for the $N = 84$ and 86 nuclei in Table I. In the $N = 84$ nuclei, the sdg-IBM
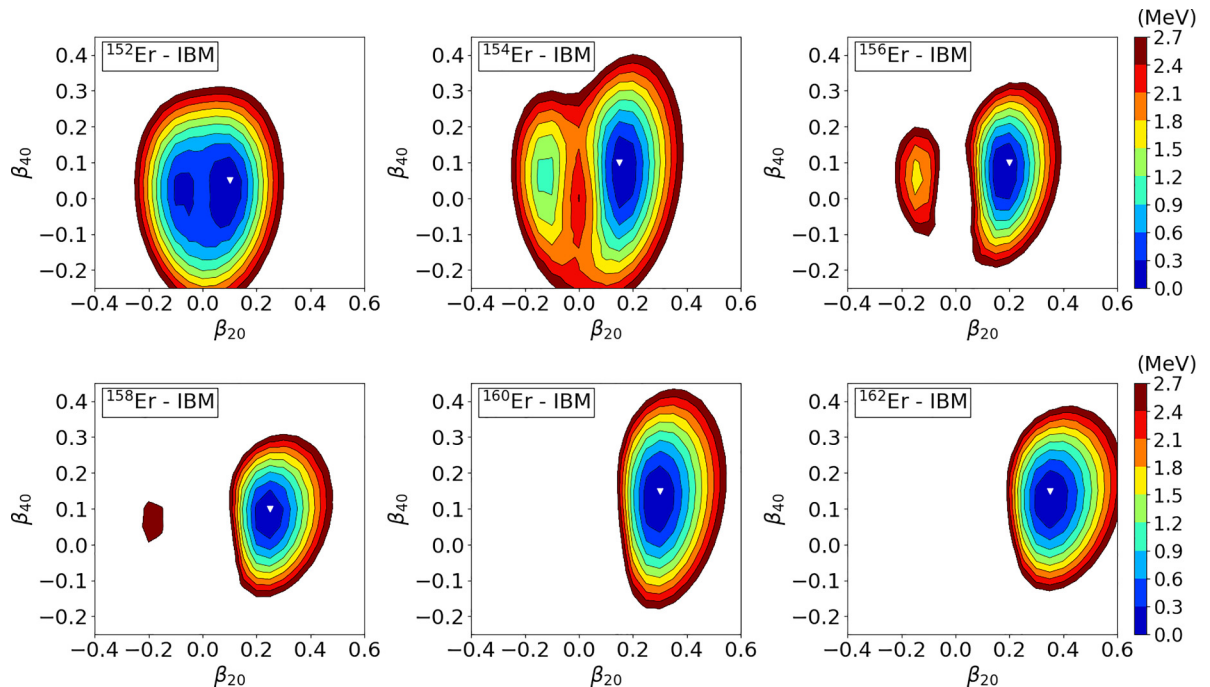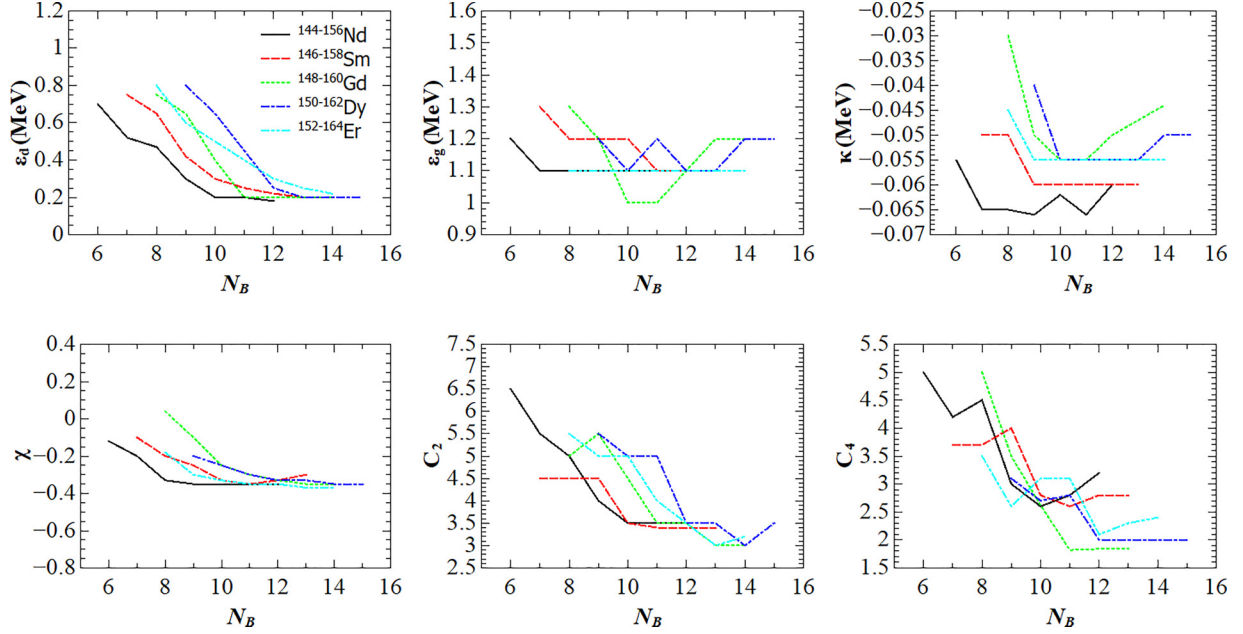

FIG. 10. Same as the caption for Fig. 1, but for the mapped sdg-IBM energy surfaces of $^{152-162}$Er.
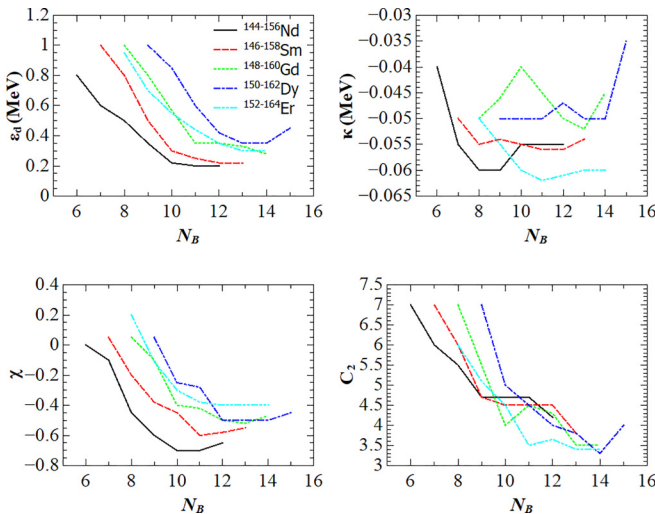
FIG. 11. Parameters of the sdg-IBM Hamiltonian (5) as functions of the boson number N_B.

predicts the ratios to be $R_{4/2} < 2$, which is in agreement with the experiment. This is also an effect of the g boson presence, since this cannot be obtained with sd-IBM calculations. A significantly low ratio, $R_{4/2} = 1.54$, is obtained for ^{152}Er, compared to the experimental value of $R_{4/2} = 1.83$. This is due to the fact that the sdg-IBM predicts the 4_1^+ state somewhat lower in energy than the experimental value. This could be improved by considering the values of the parameter σ to be $\sigma > 1.0$ for this nucleus. The calculated $R_{4/2}$ ratio that is lower than 2; nevertheless it agrees with experiment qualitatively, which, however, cannot be realized in the sd-IBM, giving $R_{4/2} = 2.14 > 2$. In the $N = 86$ nuclei, there is no significant difference between ratios obtained with

the sdg- and sd-IBM. The two exceptions are ^{146}Nd, where the sdg-IBM predicts a lower ratio, which is closer to the experimental value, and ^{148}Sm, where the sdg-IBM predicts a $R_{4/2} < 2$ value, which does not agree with the experiment.

Figure 14 compares the calculated and experimental excitation energies of the 0_2^+, 2_3^+, and 4_3^+ states, which may be associated with the $K^\pi = 0^+$ band usually present in the deformed region. Note that for ^{160}Dy the observed 0^+ level at 1280 keV, which is suggested to be the bandhead of the first excited $K = 0^+$ band, is shown in the plot [Figs. 14(g) and 14(h)], while there are two additional excited 0^+ levels at 681 and 703 keV, but with spin and parity not firmly established. As one sees in Fig. 14, the sdg-IBM does not provide an improved description of the 0_2^+ states compared to the sd-IBM, since the expectation value of the g boson number operator for the 0_2^+ state is calculated to be $\langle \hat{n}_g \rangle \approx 0$. On the other hand, the sdg-IBM predicts significantly lower

FIG. 12. Parameters of the sd-IBM Hamiltonian (10) as functions of the boson number N_B.

TABLE I. Energy ratios $R_{4/2} = E_x(4_1^+)/E_x(2_1^+)$ for the nearly spherical nuclei with $N = 84$ and 86, calculated with the mapped sd- and sdg-IBM, as compared to the experimental values [38].

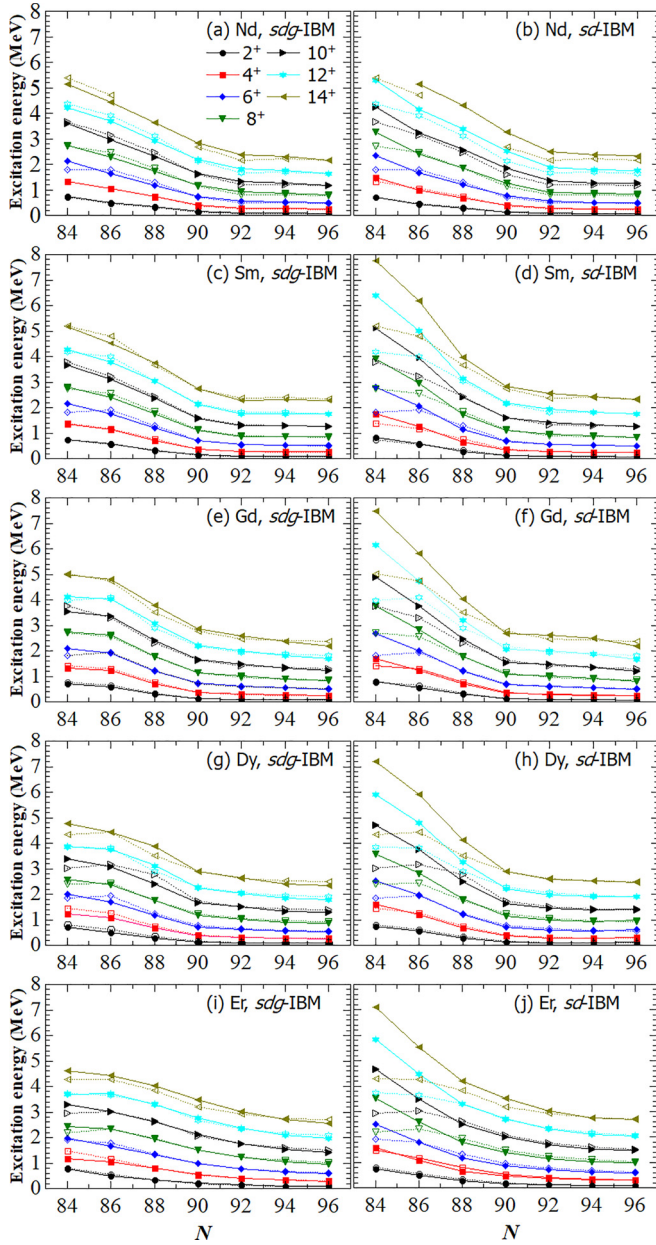| Nucleus	sd-IBM	sdg-IBM	Experiment
^{144}Nd	2.11	1.78	1.89
^{146}Nd	2.25	2.05	2.02
^{146}Sm	2.12	1.83	1.85
^{148}Sm	2.20	1.98	2.14
^{148}Gd	2.13	1.86	1.81
^{150}Gd	2.18	2.15	2.02
^{150}Dy	2.15	1.71	1.81
^{152}Dy	2.21	2.16	2.05
^{152}Er	2.14	1.54	1.83
^{152}Er	2.24	2.17	2.07

FIG. 13. Calculated excitation energies of the yrast band states up to spin $J^\pi = 14^+$ as functions of the neutron number N within the mapped sdg-IBM (left column) and sd-IBM (right column), represented by solid symbols connected by solid lines. Experimental data are taken from Ref. [38], and are depicted as open symbols connected by dotted lines.

FIG. 14. Same as Fig. 13, but for the 0_2^+, 2_3^+, and 4_3^+ states.

2_3^+ and 4_3^+ states for $N \leqslant 88$, which is in agreement with the experiment. However, in the nuclei with $N = 84$ and 86 the two states are almost equal in energy, and in the $N = 88$ nuclei the 4_3^+ state becomes lower in energy than the 2_3^+ state, which contradicts the experiment. In the $N \geqslant 90$ deformed region, both sdg- and sd-IBM yield similar results. Overall, the 2_3^+ and 4_3^+ states, calculated by the sdg-IBM, are closer in energies to the corresponding experimental values in the near shell-closure region. The sdg-IBM, however, predicts the 4_3^+ energy level to be so low as to be close to
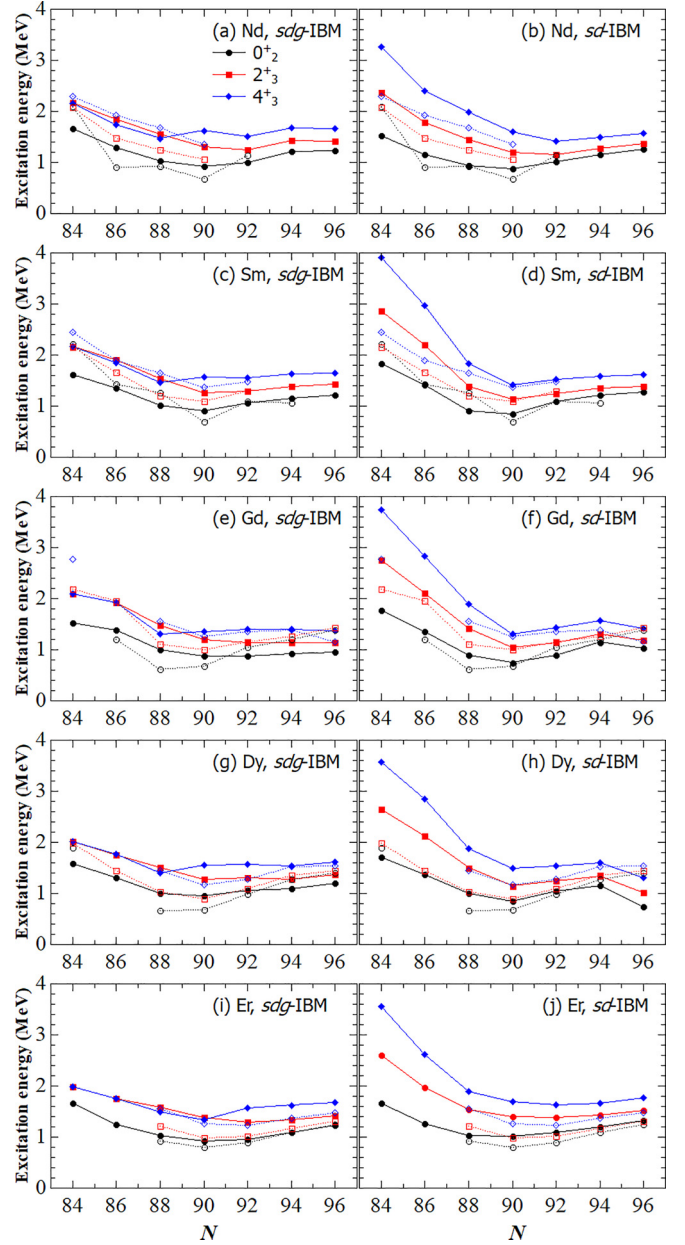
or even below the 2_3^+ one, which does not agree with the experiment. The description of 0_2^+ states is not improved in the sdg-IBM.

Figure 15 shows the excitation energies of the 2_2^+, 3_1^+, and 4_2^+ states, associated with the γ vibrational band. The effect of including g bosons on the states 2_2^+ and 3_1^+ is minor, with only some small improvements in the $N \leqslant 88$ Nd and Sm. The 4_2^+ energy level is, however, significantly low compared to the one obtained with the sd-IBM and to the observed level. In the $N = 84$ nuclei, the 4_2^+ state is predicted to be almost equal in energy to the 2_2^+ state, contrary to the experiment. In the $N \geqslant 90$ deformed region, there are no significant differences between the sdg- and sd-IBM. The fact that the sdg-IBM predicts a significantly lower 4_2^+ state compared to the experiment
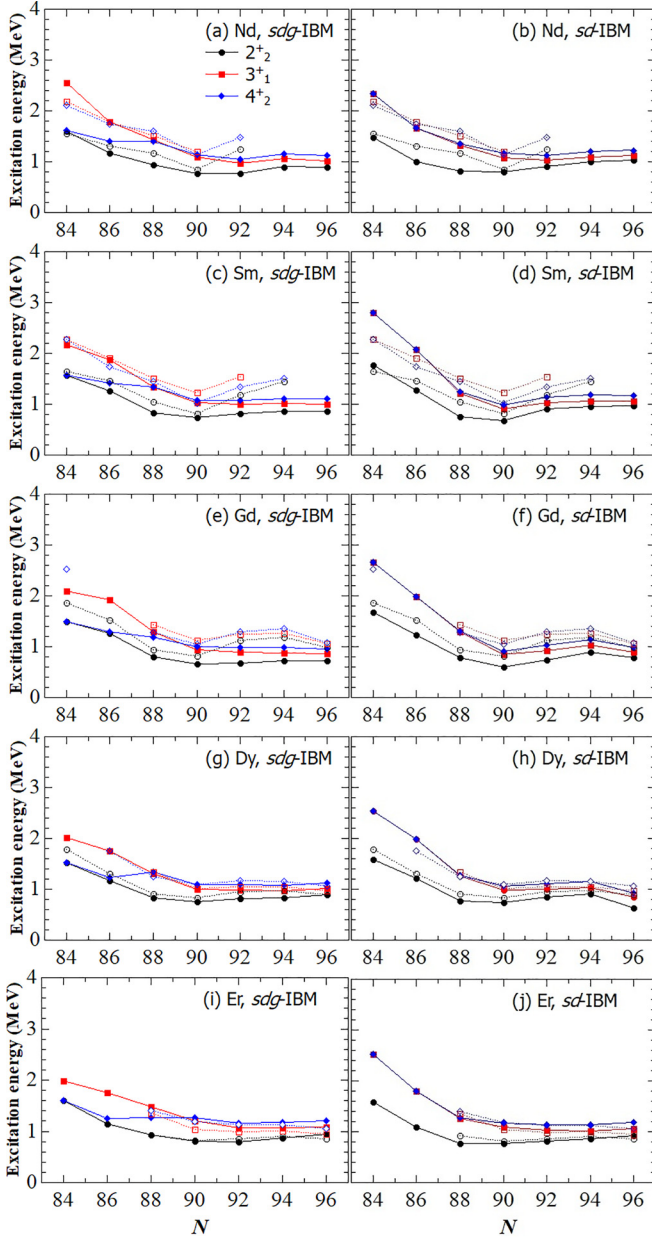
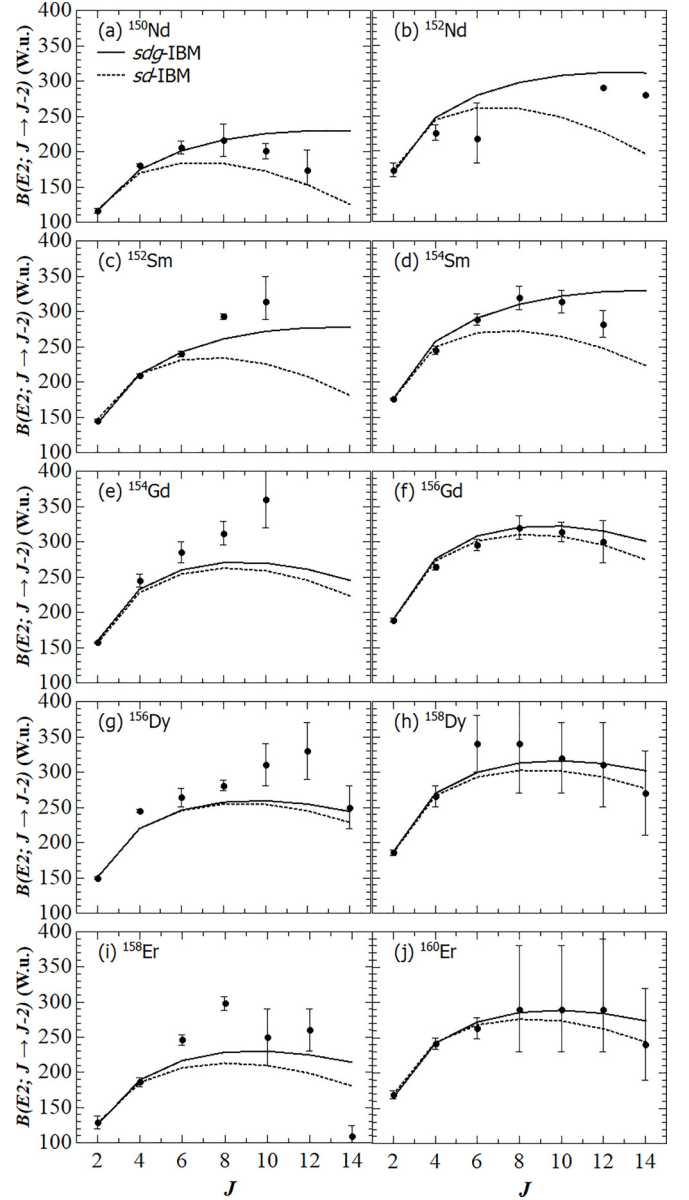FIG. 15. Same as Fig. 13, but for the 2_2^+, 3_1^+, and 4_2^+ states.

FIG. 16. $B(E2)$ transition strengths in the ground state band of the well-deformed $N = 90$ (left) and $N = 92$ (right) nuclei as functions of spin J, calculated with the mapped sdg-IBM (solid curves) and sd-IBM (dotted curves). The experimental data, represented by solid circles, are adopted from Ref. [38].

points to the fact that the chosen Hamiltonian may not be suitable for the description of such states in the region near shell closures. A Hamiltonian with more independent parameters could potentially solve this problem. However, the inclusion of more independent parameters would make the mapping procedure more involved. We also note that the choice of the EDF, as well as the choice of the pairing interaction, affects the calculated spectrum. We leave those two problems for a separate study.

B. Transition strengths

1. Quadrupole transitions

Figure 16 shows the $B(E2; J \to J - 2)$ transition strengths in the ground state bands of the well deformed $N = 90$ and

92 isotopes. We consider these isotopes due to the fact that most of the data on $E2$ transitions are available for these isotopes, which makes them the ideal cases to examine when comparing the $E2$ transition strengths between the sdg- and sd-IBM. The effective charges $e_2^{sdg,sd}$ are fitted to reproduce the experimental data on the first $B(E2; 2^+ \to 0^+)$ transition [38]. One can notice a significant difference between the behavior of the ground state band $E2$ transitions in Nd and Sm isotopes, compared to heavier ones. In Nd and Sm, the predicted transition strengths for states $J^\pi \geqslant 6^+$ are significantly larger than the sd-IBM calculated transitions, which is not the case in other isotopes. This can be explained by

the fact that in those isotopes the $(d^\dagger \times \tilde{g} + g^\dagger \times \tilde{d})^{(2)}$ term of the quadrupole operator $\hat{Q}^{(2)}$ contributes more to the calculated transitions due to the larger values of the parameter $\sigma > 1.0$. The calculated transition strengths, especially in ^{152,154}Sm, seem to correspond to the axial rotor calculations [20,42]. It can be seen that the sdg-IBM in the shown Nd and Sm isotopes improves the results of the $B(E2; J \to J-2)$ strengths for $J = 6^+, 8^+, 10^+$. In Gd, Dy, and Er isotopes, the sdg-IBM only slightly increases the $E2$ transition strengths from $J^\pi \geqslant 6^+$ states compared to the sd-IBM, which can be attributed to the fact that the value of the parameter $\sigma = 1.0$ is chosen. At $N = 90$, both models underestimate the measured transition strengths, while at $N = 92$, both models reproduce the measured strengths well. Due to the fact that the margins of error are quite large in $N = 92$ Dy and Er isotopes, it cannot be concluded whether the sdg-IBM improves the description of higher $E2$ transition strengths in those isotopes.

2. Hexadecapole transitions

Figure 17 shows the $B(E4; 4_n^+ \to 0_1^+)$ $(n = 1, 2, 3, 4)$ transition strengths. The $e_4^{sdg,sd}$ effective charges are fitted to experimental data on the $B(E4; 4_1^+ \to 0_1^+)$ from the first 4^+ state to the ground state [25–27,38]. For isotopes with no available experimental data, effective charge values are chosen so that they start from lower values, peak near $N = 92$, and then decrease again. These transition strengths are shown in Figs. 17(a) and 17(b). In Figs. 17(c)–17(h), $E4$ transition strengths from higher 4^+ states are shown. The sdg-IBM predicts several large $E4$ transition strengths from these states in certain isotopes, which is expected in the case of hexadecapole deformed nuclei with a $K = 4^+$ band. The sd-IBM predicts all of these transition strengths to vanish, which points to the necessity of considering the g boson in the description of $E4$ transitions from higher 4^+ states. Unfortunately, due to the lack of experimental data on these $E4$ transitions, it is not possible to see how well the mapped sdg-IBM predicts the values of these transition strengths.

3. Monopole transitions

Figure 18 shows the monopole strengths $\rho^2(E0; 0_i^+ \to 0_j^+)$, with $i = 2, 3$ and $j = 1, 2$, for isotopes of Sm and Gd. We choose to show these isotopes since the experimental data on monopole strengths is only available for these isotopes [38,44]. The choice of $\eta = \gamma = 0.75$ fm^2 is made to reproduce most of the available experimental data. The sdg-IBM does not significantly improve the calculated monopole strengths compared to the sd-IBM. Both models overestimate the strengths of $0_2^+ \to 0_1^+$ transitions in ^{150,152}Sm and underestimate the same strength in ^{154}Gd. The calculated strengths of ^{154}Sm and ^{152,156}Gd are within the margins of error of the measured strengths. The sdg-IBM does slightly improve the description of the $0_3^+ \to 0_2^+$ transition in ^{154}Sm and the $0_3^+ \to 0_1^+$ transition in the ^{158}Gd. Overall, the sdg-IBM does not differ significantly from the sd-IBM in the description of the monopole strengths, which is expected,
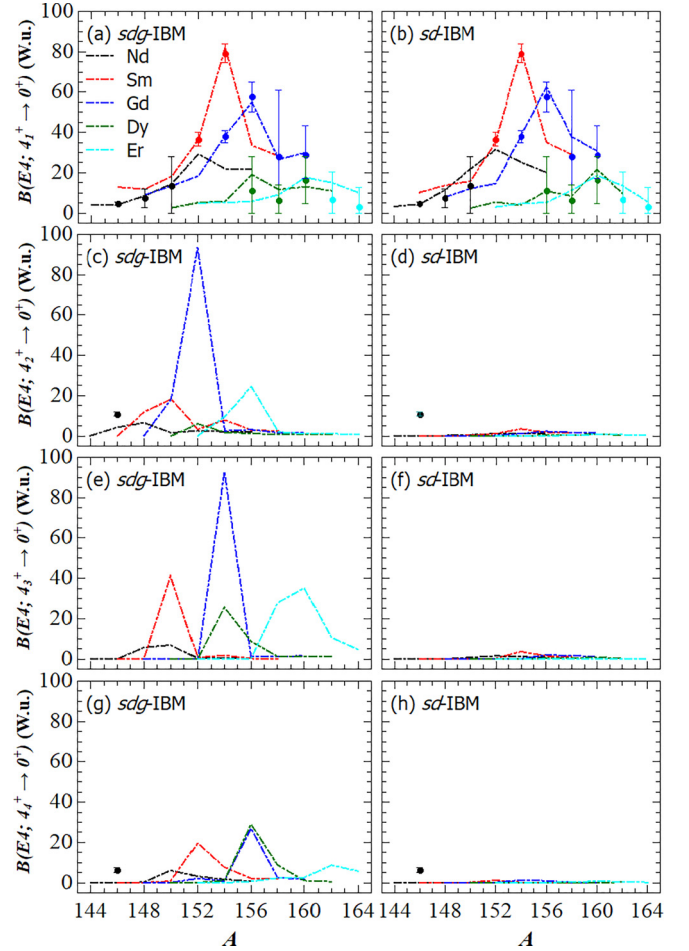

FIG. 17. $B(E4)$ strengths in W.u. for the transitions of the first [panels (a) and (b)], second [panels (c) and (d)], third [panels (e) and (f)], and fourth [panels (g) and (h)] 4^+ states to the 0_1^+ ground state as functions of the mass number A, calculated with the mapped sdg-IBM (left column) and sd-IBM (right column). Experimental data are taken from Refs. [25–27,38], and are indicated by solid circles in the plots.

since the sdg-IBM calculations do not predict a presence of g bosons in 0^+ states up to 0_3^+. For example, in ^{154}Sm, the lowest 0^+ state that contains one g boson, with the expectation value $\langle \hat{n}_g \rangle \approx 1$, is the 0_5^+ state. In principle, it is possible to fit η and γ separately for each isotope. However, since our goal was to see the effect of g bosons in monopole transitions, we follow the method of [37] and set fixed values of η and γ parameters.

V. SUMMARY

We have shown an extended analysis of the impact of hexadecapole deformations on the excitation energy spectra and transition strengths in even-even rare-earth nuclei, ranging from the near spherical to the well deformed ones. The quadrupole-hexadecapole constrained SCMF PES has been mapped onto the corresponding PES of the IBM, and this procedure completely determines the parameters of the sdg-IBM Hamiltonian, based on the microscopic calculations. The inclusion of g bosons has a significant effect on $J^\pi \geqslant 6^+$
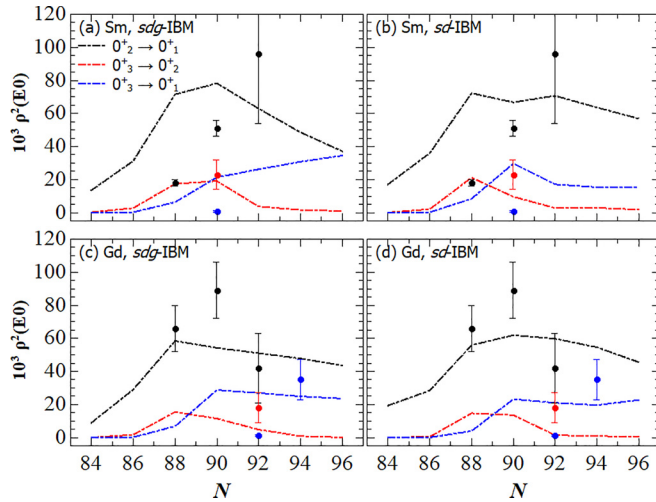
FIG. 18. $\rho^2(E0; 0^+_i \to 0^+_j)$ values as functions of the neutron number N for Sm and Gd isotopes, calculated with the mapped sdg-IBM (left column) and sd-IBM (right column). Experimental values are adopted from Refs. [38,44], and are plotted as solid circles.

yrast states in the $N \leqslant 88$ nuclei near neutron magic number $N = 82$. The mapped sdg-IBM lowers the energies of aforementioned states to agree with the observed spectra. In the case of non-yrast states and corresponding bands, the sd-IBM seems to be sufficient in the description of such states, with the sdg-IBM making only a minor contribution, e.g., 2^+_3 and 4^+_3

states of the $K^\pi = 0^+$ band in the $N = 84$ and 86 nuclei. As for the transitions, in the well deformed nuclei with $N = 90$ and 92, the sdg-IBM calculation yields higher $B(E2; J \to J - 2)$ values for $J^\pi \geqslant 6^+$ yrast states, which does seem to be an improvement of the results, especially in the case of ^{150,152}Nd and ^{152,154}Sm. In the case of monopole transitions between 0^+ states, the effect of the g boson seems to be minor. In the well deformed region, the sdg-IBM predicts the existence of the $K^\pi = 4^+$ band with an enhanced $B(E4; 4^+ \to 0^+)$ hexadecapole transition to the ground states. The fact that the sd-IBM cannot predict larger hexadecapole transition strengths from higher 4^+ states points to a necessity of including the g boson in the description of the hexadecapole transitions. Unfortunately, due to the lack of experimental data on such transitions, it is not possible to see how well the sdg-IBM reproduces such transitions. Now that we have shown the usefulness of the mapped sdg-IBM, we can expand our study to the even-odd and odd-odd rare-earth nuclei, as well as extend our model to the more complex sdg-IBM-2 to study properties such as scissors modes in rare-earth nuclei. It could also be interesting to systematically study how sensitive the parameters are to the choice of the EDF in the SCMF calculations.

ACKNOWLEDGMENTS

[1] A. Bohr and B. R. Mottelson, *Nuclear Structure* (Benjamin, New York, USA, 1975), Vol. II.

[2] P. Ring and P. Schuck, *The Nuclear Many-Body Problem* (Springer-Verlag, Berlin, 1980).

[3] Y. K. Gupta, B. K. Nayak, U. Garg, K. Hagino, K. B. Howard, N. Sensharma, M. Şenyiğit, W. P. Tan, P. D. O'Malley, M. Smith, R. Gandhi, T. Anderson, R. J. deBoer, B. Frentz, A. Gyurjinyan, O. Hall, M. R. Hall, J. Hu, E. Lamere, Q. Liu *et al.*, Phys. Lett. B **806**, 135473 (2020).

[4] W. Ryssens, G. Giacalone, B. Schenke, and C. Shen, Phys. Rev. Lett. **130**, 212302 (2023).

[5] J. H. Chi, Y. Qiang, C. Y. Gao, and J. C. Pei, Nucl. Phys. A **1032**, 122626 (2023).

[6] J. Engel and J. Menéndez, Rep. Prog. Phys. **80**, 046301 (2017).

[7] F. Iachello and A. Arima, *The Interacting Boson Model* (Cambridge University Press, Cambridge, 1987).

[8] R. F. Casten and D. D. Warner, Rev. Mod. Phys. **60**, 389 (1988).

[9] K. Nomura, N. Shimizu, and T. Otsuka, Phys. Rev. Lett. **101**, 142501 (2008).

[10] K. Nomura, N. Shimizu, and T. Otsuka, Phys. Rev. C **81**, 044307 (2010).

[11] K. Nomura, T. Otsuka, R. Rodríguez-Guzmán, L. M. Robledo, and P. Sarriguren, Phys. Rev. C **83**, 014309 (2011).

[12] K. Nomura, N. Shimizu, D. Vretenar, T. Nikšić, and T. Otsuka, Phys. Rev. Lett. **108**, 132501 (2012).

[13] K. Nomura, D. Vretenar, and B.-N. Lu, Phys. Rev. C **88**, 021303(R) (2013).

[14] K. Nomura, D. Vretenar, T. Nikšić, and B.-N. Lu, Phys. Rev. C **89**, 024312 (2014).

[15] T. Otsuka, Nucl. Phys. A **368**, 244 (1981).

[16] T. Otsuka, A. Arima, and N. Yoshinaga, Phys. Rev. Lett. **48**, 387 (1982).

[17] T. Otsuka and J. N. Ginocchio, Phys. Rev. Lett. **55**, 276 (1985).

[18] T. Otsuka and M. Sugita, Phys. Lett. B **209**, 140 (1988).

[19] Y. D. Devi and V. K. B. Kota, Z. Phys. A **337**, 15 (1990).

[20] S. Kuyucak, Nucl. Phys. A **570**, 187 (1994).

[21] P. Van Isacker, A. Bouldjedri, and S. Zerguine, Nucl. Phys. A **836**, 225 (2010).

[22] L. Lotina and K. Nomura, Phys. Rev. C **109**, 034304 (2024).

[23] D. L. Hendrie, N. K. Glendenning, B. G. Harvey, O. N. Jarvis, H. H. Duhm, J. Saudinos, and J. Mahoney, Phys. Lett. B **26**, 127 (1968).

[24] K. A. Erb, J. E. Holden, I. Y. Lee, J. X. Saladin, and T. K. Saylor, Phys. Rev. Lett. **29**, 1010 (1972).

[25] H. J. Wollersheim and T. W. Elze, Nucl. Phys. A **278**, 87 (1977).

[26] R. M. Ronningen, J. H. Hamilton, L. Varnell, J. Lange, A. V. Ramayya, G. Garcia-Bermudez, W. Lourens, L. L. Riedinger,

F. K. McGowan, P. H. Stelson, R. L. Robinson, and J. L. C. Ford, Phys. Rev. C **16**, 2208 (1977).

[27] R. M. Ronningen, R. B. Piercey, J. H. Hamilton, C. F. Maguire, A. V. Ramayya, H. Kawakami, B. van Nooijen, R. S. Grantham, W. K. Dagenhart, and L. L. Riedinger, Phys. Rev. C **16**, 2218 (1977).

[28] S. Hilaire and M. Girod, Eur. Phys. J. A **33**, 237 (2007).

[29] S.-G. Zhou, Phys. Scr. **91**, 063008 (2016).

[30] B.-N. Lu, J. Zhao, E.-G. Zhao, and S.-G. Zhou, Phys. Rev. C **89**, 014323 (2014).

[31] J. Zhao, B.-N. Lu, E.-G. Zhao, and S.-G. Zhou, Phys. Rev. C **95**, 014320 (2017).

[32] D. Vretenar, A. V. Afanasjev, G. A. Lalazissis, and P. Ring, Phys. Rep. **409**, 101 (2005).

[33] T. Nikšić, D. Vretenar, and P. Ring, Prog. Part. Nucl. Phys. **66**, 519 (2011).

[34] T. Nikšić, D. Vretenar, and P. Ring, Phys. Rev. C **78**, 034318 (2008).

[35] Y. Tian, Z. Y. Ma, and P. Ring, Phys. Lett. B **676**, 44 (2009).

[36] V. K. B. Kota, J. V. der Jeugt, H. D. Meyer, and G. V. Berghe, J. Math. Phys. **28**, 1644 (1987).

[37] S. Zerguine, P. Van Isacker, and A. Bouldjedri, Phys. Rev. C **85**, 034331 (2012).

[38] Brookhaven National Nuclear Data Center, http://www.nndc.bnl.gov.

[39] W. Nazarewicz and P. Rozmej, Nucl. Phys. A **369**, 396 (1981).

[40] E. Ganioğlu, R. Wyss, and P. Magierski, Phys. Rev. C **89**, 014311 (2014).

[41] C. V. N. Kumar and L. M. Robledo, Phys. Rev. C **108**, 034312 (2023).

[42] S. Kuyucak and V.-S. Lac, Phys. Rev. C **47**, 1815 (1993).

[43] S. Heinze, computer program ARBMODEL, University of Cologne, 2008, https://d-nb.info/989617858/34.

[44] T. Kibédi and R. H. Spear, At. Data and Nucl. Data Tables **89**, 77 (2005).